Structural basis of the Cope rearrangement and cyclization in hapalindole biogenesis

AUTHORS

Sean A. Newmister[1], Shasha Li[1,2], Marc Garcia-Borràs[3], Jacob N. Sanders[3], Song Yang[3], Andrew N. Lowell[1], Fengan Yu[1], Janet L. Smith[1,4], Robert M. Williams[5,6], K. N. Houk[3]*, David H. Sherman[1,2,7,8]*

AFFILIATIONS

[1]Life Sciences Institute, University of Michigan, Ann Arbor, MI 48109, USA

[2]Department of Medicinal Chemistry, University of Michigan, Ann Arbor, MI 48109, USA

[3]Department of Chemistry and Biochemistry, University of California, Los Angeles, CA 90095, USA

[4]Department of Biological Chemistry, University of Michigan, Ann Arbor, MI 48109, USA

[5]Department of Chemistry, Colorado State University, Fort Collins, CO 80523, USA

[6]University of Colorado Cancer Center, Aurora, CO 80045, United States

[7]Department of Chemistry, University of Michigan, Ann Arbor, MI 48109, USA

[8]Department of Microbiology & Immunology, University of Michigan, Ann Arbor, MI 48109, USA

*Corresponding authors. Email: davidhs@umich.edu (D.H.S.); houk@chem.ucla.edu (K.N.H.)

ABSTRACT

Hapalindole alkaloids are a structurally diverse class of cyanobacterial natural products defined by their varied polycyclic ring systems and diverse biological activities. These complex metabolites are generated from a common biosynthetic intermediate by the Stig cyclases in three mechanistic steps, including a rare Cope-rearrangement, 6-*exo*-*trig* cyclization, and electrophilic aromatic substitution. Here we report the structure of HpiC1, a Stig cyclase that catalyzes the formation of 12-*epi*-hapalindole U in vitro. The 1.5 Å structure reveals a dimeric assembly with two calcium ions per monomer and the active sites located at the distal ends of the protein dimer. Mutational analysis and computational methods uncovered key residues for an acid catalyzed [3,3]-sigmatropic rearrangement and specific determinants that control the position of terminal electrophilic aromatic substitution leading to a switch from hapalindole to fischerindole alkaloids.

INTRODUCTION

The hapalindole family of alkaloids are a large and structurally diverse class of natural products from cyanobacteria of the order *Stigonematales*[1]. These metabolites are active against a broad range of targets, which include antibacterial, antifungal, insecticidal, and antimitotic activities[2-7]. Each member is classified as a hapalindole, ambiguine, fischerindole, or welwitindolinone based on its core ring system (Supplementary Fig. 1), and they have been the subject of various total syntheses due to their structural complexity and unique biological properties[1]. Until recently comparatively little was known regarding the biogenesis of these alkaloids, and particularly the construction of the tetracyclic core ring system.

Initial reports demonstrated that hapalindoles are derived from *cis*-indole isonitrile and geranyl pyrophosphate (GPP)[8-10], but the biogenesis of the polycyclic ring systems remained elusive. We recently identified an unexpected biosynthetic intermediate **1** that undergoes a Cope rearrangement followed by a cyclization cascade to generate 12-*epi*-hapalindole U (**5**) (Fig. 1)[11]. The Cope rearrangement is a 3,3-sigmatropic rearrangement that proceeds through a cyclic transition state (Fig. 1)[12]. Although this pericyclic reaction is prevalent in organic synthesis[13], it has rarely been identified as a biosynthetic transformation[14-16]. The biosynthesis of **5** was proposed to proceed through a three-part reaction mechanism: (1) Cope rearrangement of **1** to generate intermediate 3, which sets the stereochemistry at positions C11 and C12; (2) 6-*exo*-*trig* cyclization of 3 to intermediate 4, which sets the stereochemistry at positions C10 and C15; and (3) electrophilic aromatic substitution of 4 to give **5** upon deprotonation (Fig. 1*b*). This discovery was expanded to include several Stig cyclases and revealed that the variant configurations observed in this class of alkaloids are generated from a central biosynthetic intermediate **1**, transformed to products in a regio- and stereospecific fashion by various members of the cyclase family (Fig. 1)[17-19]. Notably, FimC5, which gives the major product 12-*epi*-fischerindole U (**6**), generates a product with a stereochemical configuration identical to **5** at C10, C11, C12 and C15, but differs in the site of C-ring attachment to the indole moiety. This indicates that the enzymes direct the site of terminal electrophilic aromatic substitution, thereby providing the regiochemical control that differentiates the hapalindoles and fischerindoles. Both HpiC1 and FimC5 produce low levels of tricyclic 12-epi-

hapalindole C (**7**), a shunt metabolite that is not converted to its tetracyclic congeners by either enzyme. Thus, biogenesis of hapalindole-type metabolites includes a fascinating mechanistic puzzle regarding how homologous Stig cyclases maintain stereochemical and regiochemical control at each of these biosynthetic steps in the formation of varied hapalindoles and fischerindoles.

In this study, we describe the molecular basis for the Stig cyclase ability to control three reactions. Originally annotated as unknown proteins[8], no information was available regarding the structure of this new type of biosynthetic enzyme. We describe herein the first crystal structure of a Stig cyclase, HpiC1, and show through a mutational analysis that localizes its active site the ability to reconfigure its metabolite profile. Density functional calculations on the mechanism and molecular dynamics simulations provide detailed information on the enzymatic processes that control product formation. These data provide compelling insights into the mechanism of Cope rearrangement, 6-*exo*-*trig* cyclization and electrophilic aromatic substitution for this class of natural products.

RESULTS

Structure of HpiC1.

Following recent work that reported the function and selectivity of Stig cyclase proteins[11,17-19], we sought a structure of HpiC1 to understand the structural basis of the complex cyclization cascade of **1**, and to understand how the Stig cyclases catalyze formation of variant alkaloid products from this common biosynthetic intermediate. We obtained HpiC1 crystals in four different forms, under conditions with varied Ca^{2+} concentration. These forms reveal the same overall structure for HpiC1, but differ in their space group, indicating that Ca^{2+} concentration can influence crystal packing (see below). The 1.7 Å structure in Form 1 was solved by selenomethionyl SAD phasing from a HpiC1 W73M/K132M double mutant, as the wild-type protein lacks Met. The SeMet W73M/K132M structure was used to solve structures in the other crystal forms by molecular replacement (Supplementary Table 1). The overall fold of the HpiC1 polypeptide is a flattened β-jelly roll fold (Fig. 2*a*) composed of two antiparallel β-sheets. The antiparallel pairing of strands β6 in two monomers creates a continuous β-sheet across an extensive dimer interface, which buries 2060 $Å^2$ of total surface area (PISA, Fig. 2*b*)[20], and encompasses

approximately 20% of the total surface area of each monomer. This arrangement is consistent with size exclusion chromatography in which HpiC1 and other Stig cyclases migrated as apparent dimers[17]. HpiC1 shares highest structural similarity (2.3 Å rmsd, DALI[21]) with the carbohydrate-binding module (CBM) from xylanase in the thermostable bacterium *Rhodothermus marinus* (PDBid: 2Y64, Fig. 2*c*)[22]. The proteins have highly similar tertiary structure and topology with the most significant differences occurring at their N-termini and in the loop regions between shared β-strands.

HpiC1 has two integral Ca^{2+} ions, each with octahedral coordination geometry (Supplementary Fig. 2). These sites were a key starting point to assess the structural and catalytic role that Ca^{2+} plays in the Stig cyclase enzymes. In vitro assays conducted in the presence of 5 mM EDTA showed no activity, which confirmed that Ca^{2+} is required for catalytic function in HpiC1[18]. From sequence comparisons, we expect the integral calcium-binding sites and the core dimeric assembly to be maintained in the other Stig cyclase enzymes (Supplementary Fig. 3).

HpiC1 active site identification.

The substrate-free HpiC1 structure did not immediately suggest the location of substrate binding and catalysis. Initial localization of the active site was revealed by abnormal electron density in a pocket located at the distal end of each subunit. Polyethylene glycol from the crystallization was modeled into this pocket (Supplementary Fig. 4), which was composed of numerous aromatic amino acids (Fig. 3). Given the hydrophobicity of substrate **1**, we explored whether this hydrophobic pocket could be the active site. This region was probed using Autodock VINA with **5** (Fig. 1)[23]. The major product was chosen based on its defined stereochemistry and rigid scaffold. The top docking solutions had affinities ranging between -9.7 and -9.4 kcal/mol (Supplementary Fig. 5), which suggested that this site possesses an appropriate size and shape to accommodate the hapalindole core.

The docking solutions compelled us to further interrogate this region as the putative active site. First, we probed the catalytic role of HpiC1 D214. This residue is 100% conserved in all of the currently identified Stig cyclases and is exceptional as the amino acid in the hydrophobic pocket most likely to participate in acid/base chemistry, which can be inferred to promote [3,3]-sigmatropic rearrangments[24].

The D214 carboxylate lacks a counter-ion and is hydrogen bonded to the Y89 hydroxyl. Substitution of D214 to alanine abolished activity (Fig. 4), indicating that it plays a critical role in the catalytic cascade. The corresponding N214 and E214 variants were also completely inactive (Supplementary Fig. 6). These results provide compelling evidence that this hydrophobic pocket is the enzyme active site.

The enzyme conformation about D214 varies among the crystal forms (Supplementary Fig. 7). In Form 1 D214 is shielded by F138, whereas this residue is shifted in Forms 2, 3, and 4 to expose D214 to the binding pocket. The loop containing F138 is also shifted ~3 Å from its position in Form 1, although coordination of the calcium ion by the carbonyl oxygen of F138 is maintained. The atomic temperature factors in this region also indicate a higher degree of mobility (Supplementary Fig. 8). It is apparent that conformational flexibility would be required to perform multiple catalytic steps in a single binding site, and also to accommodate the broad range of regio- and stereochemical configurations in this class of alkaloids[1].

Altered product profile through mutagenesis.

Based on the different product profiles of the various Stig cyclases, we examined the conservation of residues in this hydrophobic pocket. Comparison revealed that sequence clustering correlates to similar product profiles. We reasoned that key determinants of cyclase reactivity were contained within these localized sequences (Fig. 3), and this site was explored by mutagenesis. A comparative analysis between HpiC1 and FimC5 (68% sequence identity with HpiC1, catalyzes **6** production from **1**) was pursued based on their ability to differentially produce hapalindole or fischerindole core ring systems, respectively (Fig. 1)[17]. Remarkably, substitution of F138 in HpiC1 to the corresponding serine from FimC5 led to the generation of a mixture of its major product, hapalindole **5**, and the FimC5 major product, fischerindole **6** (Fig. 4). The product ratio in F138S is approximately 1:2 (**6**:**5**) and is shifted to 2:1 (**6**:**5**) in Y101F/F138S. HpiC1 Y101F had a comparable product profile to wild-type protein, indicating that this effect is driven primarily by F138. A corresponding mutation at this position in FimC5, S139F, did not lead to formation of **5**; instead the product profile was shifted towards the production of **7**, a minor tricyclic shunt product

of the native HpiC1 and FimC5 reactions (Supplementary Fig. 9)[17]. These data indicate that both HpiC1 F138 and FimC5 S139 play a key role in directing terminal electrophilic aromatic substitution.

Mutations guided by sequence alignments were introduced into HpiC1 to identify additional key residues (Fig. 3). The Y101S/F138S variant that corresponds to the FamC3/HpiC3/FilC3 homologs showed no activity with **1** (Fig. 4), which is consistent with the lack of reactivity observed in homodimeric forms of FamC3/HpiC3/FilC3[17]. HpiC1 Y101S also showed reduced activity, though to a lesser extent than in combination with F138S. Intriguingly, FamC3 was shown to associate with FamC2 as a heterodimer, and catalyze the formation of hapalindole H[17].

In order to understand the impact of these mutations, high resolution structures were determined for HpiC1 variants Y101F, Y101S, F138S, and Y101F/F138S. While our efforts to observe bound ligands by either soaking or co-crystallization only afforded complexes with DMSO and Tris buffer (Supplementary Fig. 4), these structures aided our efforts to interrogate the mechanism of cyclization in HpiC1 using computational methods.

Molecular Dynamics of HpiC1.

We first applied molecular dynamics (MD) simulations to the substrate-free structures to gain insights into the dynamics of the active site. Starting from the apo HpiC1 dimeric structure, analysis of the MD trajectories revealed large fluctuations of the loop containing F138 (N137-F150) (Supplementary Fig. 10), in agreement with the different conformations found for this loop in the crystal structures (Supplementary Fig. 7). MD simulations show that D214, which is essential for enzyme activity, stays preferentially in a conformation in which the D214 side chain points towards the inner cavity of the active site, while F138 acts as a wall on the side of the active site pocket (Supplementary Fig. 11). This is due in part to the Y89 hydroxyl H-bond with the D214 carboxylic acid group (Supplementary Fig. 11-12). Importantly, the predicted pKa for D214, estimated from snapshots obtained along 500ns of MD simulation (Supplementary Fig. 13), is 6.5 - 7.0, indicating that it can be protonated in an acid-base equilibrium to act as a protonating species during catalysis. An alternative conformation of F138 is sampled during the 500 ns trajectory. In this conformation, the F138 side chain is displaced and D214 becomes inaccessible,

generating an inactive conformation (Supplementary Fig. 11-12) that is similar to the arrangement observed in the crystal Form 1 (Supplementary Fig. 7).

We considered the lack of activity in the Y101S/F138S mutant. MD simulations for Y101S/F138S showed that Y101S interacts closely with D214, in addition to the Y89 hydroxyl H-bond (Supplementary Fig. 14-15). These two H-bonds favor stabilization of a negatively charged carboxylate group, which will not be protonated in this more polar environment. This is confirmed by the decrease of the predicted pKa value of D214 (pKa ≈ 5.5 - 6) (Supplementary Fig. 13).

As described above, F138S and Y101F/F138S mutants change the product profile in HpiC1 leading to increased formation of fischerindole **6** (Fig. 4). We performed 500 ns MD simulations on both F138S and Y101F/F138S mutants, finding important changes in the active site shape. The F138S mutation creates more space around the catalytic D214 residue and also releases the interaction between the two phenyl rings of F138 and F210, with F210 becoming more flexible (Supplementary Fig. 16). This active site reshaping is responsible for the change in the reaction outcome, as discussed below.

QM analysis of three-part mechanism.

We employed density functional theory (DFT) calculations to explore the possible reaction mechanism for Stig cyclases, in particular the Cope rearrangement, which is the first step in the three-part reaction cascade starting from **1**[11]. The instability of **1** has precluded determining its chiral configuration at the indolenine C3 position. Thus, we computed the Cope rearrangement and cyclization cascade mechanism (Fig. 5) starting from both the (*R*)-**1** and (*S*)-**1** enantiomers (Supplementary Fig. 17).

Although a typical Cope rearrangement has four possible transition states, two chairs and two boats (Supplementary Fig. 18-19), only one chair-like transition state can account for the known stereochemistry at C11 and C12 in the products and, therefore, only this transition state was further considered. Given that the active site of HpiC1 contains the essential D214 residue, we explored the impact of this residue on accelerating the Cope rearrangement. The conversion of neutral starting material 1(*R*)N to intermediate 3N is concerted, proceeding through a single chair-like transition state 2N, which lies 20.6 kcal/mol above the near attack conformation (NAC) of the starting material. This chair-like

transition structure (Supplementary Fig. 20) has dissociative character, with breaking and forming partial single bonds of 2.58 Å and 2.53 Å, respectively. The partial negative charge on the isocyanidovinylindolenine fragment of –0.43 *e* can be stabilized by a hydrogen bonding donor at the indolenine nitrogen, which has a partial negative charge of –0.49 *e*. Adding an acetic acid molecule to mimic possible hydrogen-bonding between D214 and the indolenine nitrogen lowers this barrier by 2.2 kcal/mol (40-fold rate enhancement), with the conversion of 1(*R*)A to 3A proceeding through a chair-like transition state 2A with a free energy barrier of 18.4 kcal/mol. These computations suggest that D214 could facilitate the Cope rearrangement by hydrogen-bonding to the indolenine nitrogen. Fully protonating the indolenine nitrogen, which represents the maximum limit of potential acid catalysis by D214, results in a change of mechanism. The conversion from 1(*R*)P to 3P is stepwise and dissociative, with 2P being an intermediate rather than a transition state, and has a much lower overall free energy barrier of 6.8 kcal/mol. Intermediate 2P is stabilized by full conjugation between the indole and isonitrile groups, and by an allylic cation to produce this much lower overall barrier (Fig. 5).

The second proposed step in the biosynthesis of **5** and **6** is the 6-*exo*-*trig* cyclization of intermediate 3 to 4, which sets the stereochemistry at C10 and C15 in the products. In gas-phase DFT optimizations, it was possible to locate a transition state for this cyclization only when the indolenine nitrogen was protonated. Without protonation, the zwitterionic character of the possible transition state leads to bond formation between negatively-charged position C3 of the indolenine and positively-charged position C16 to generate a cyclobutane ring. In contrast, the protonated species undergoes facile cyclization from 3P to intermediate 4P through a low-lying transition state. This suggests that protonation is crucial and that D214 may catalyze cyclization in this way, and possibly the preceding Cope rearrangement as well.

The third step is electrophilic aromatic substitution of intermediate 4P, with two different transition states leading to the two major products. Electrophilic aromatic substitution at C4 of the indole yields intermediate 5P, which gives **5** upon deprotonation, while electrophilic aromatic substitution at C2 of the indole yields intermediate 6P, which gives **6** upon deprotonation. Deprotonation at C16 can lead to formation of tricyclic **7** (Fig. 1), which is generated as a trace product by HpiC1. QM calculations show

that formation of **6**, which has the lower-energy transition state, should be intrinsically favored. Thus, the regioselectivity of electrophilic aromatic substitution to generate **5** appears to be controlled by the HpiC1 active site as opposed to inherent energetics of the system.

MD simulations with modeled ligands.

To understand enzymatic control of the Cope rearrangement, we conducted 500 ns MD simulations on wild-type HpiC1 with both 1(*R*)P and 1(*S*)P bound into the active site (Supplementary Fig. 21). Both enantiomers retain the key H-bond interaction between the protonated indolenine NH and the D214 residue (Supplementary Fig. 21). However, the C11-C12 distance, which corresponds to the C-C bond formed during the Cope rearrangement, is shorter (~3.5Å) for the 1(*R*)P substrate than for the 1(*S*)P substrate (>4.0Å). In addition, only 1(*R*)P is stabilized by the enzyme active site in a near attack conformation (NAC) that leads to the correct stereochemistry at positions 11 and 12 (Fig. 6*a-b*, Supplementary Fig. 21-22). Based on these observations, the (*R*) enantiomer of **1** is the most plausible natural substrate.

To understand how HpiC1 could control the differentiation of hapalindole/fischerindole products we performed MD simulations with intermediates prior to electrophilic aromatic substitution. We considered the two intermediate precursors 4P and 10P that derive from the 1(*R*)P and 1(*S*)P starting materials, respectively. Since either 4P or 10P can generate both the **5** and **6** products, we analyzed the binding of both intermediates. MD simulations with the two docked intermediates show that 4P more effectively maintains the H-bond between the protonated NH-indole and D214 than 10P, which rapidly dissociates during the simulation (Supplementary Fig. 23). These results reinforce the idea that **1**(*R*) is the most plausible natural substrate. Moreover, MD simulations showed that when 4P is bound into the active site, it adopts a conformation in which the distance between C4 and C16 (~3.5Å; corresponds to hapalindole formation) is shorter than the distance between C2 and C16 (~4.0Å; corresponds to fischerindole formation) (Fig. 6*c*, Supplementary Fig. 23). Finally, around 200 ns a conformational change of the F138 side chain reverses this trend to disrupt the interaction of 4P and D214 (Supplementary Fig. 23-24), highlighting the key role of F138 residue in controlling the site-selectivity of the reaction.

The critical role of F138 was investigated through MD simulations on the F138S and Y101F/F138S mutants with 4P. In both trajectories, the distance between C2 and C16 leading to fischerindole formation is shortened compared to wild-type enzyme, becoming closer (~3.5Å) than the distance between C4 and C16 (~4.0Å) leading to hapalindole formation, consistent with the experimentally observed product ratios (Fig. 6*d*, Supplementary Fig. 26). The absence of the bulky F138 residue near C2 allows the intermediate to adopt a slightly different conformation enabling formation of **6** without completely suppressing generation of **5** (Fig. 6*d*, Supplementary Fig. 27).

As with the terpene cyclases[25-27], aromatic side chains in HpiC1 are appropriately positioned to form cation–π interactions with the carbocation of 4P. Examination of the MD trajectories shows that F138 and F142 can interact with the C16 carbocation, while F88 and F210 are either too far away or poorly oriented for interaction (Supplementary Fig. 25)[28]. An aromatic amino acid F142 is conserved in all known Stig cyclases, whereas F138 is varied with different product outcomes as observed in our mutational analysis and calculations.

DISCUSSION

The structure of HpiC1 has provided the first high resolution insights into a fascinating mechanistic puzzle in which the Stig cyclases are able to generate extensive stereochemical and regiochemical diversity through the common biosynthetic precursor **1**. The surprising function of the Stig cyclases[11] could not be inferred from bioinformatic analysis, and similarly, structural and mechanistic insights from homology-based tools were unavailable for these remarkable biocatalysts. HpiC1 is not homologous with any characterized terpene cyclase, but instead is most similar to bacterial carbohydrate binding modules (CBM). CBMs function primarily to bring various hydrolytic enzymes into contact with their carbohydrate substrates. Target sugar molecules bind the CBMs in an extended cleft at the protein surface, which is mediated through several amino acids that are not conserved in HpiC1 (Fig. 2*c*)[22]. This indicates a divergent functionality in HpiC1 based on a shared protein scaffold. Nevertheless, Stig cyclases and CBMs share several properties including a common fold, thermostability (Supplementary

Fig. 28)[29], and structural calcium ions, which play an important role in CBM stabilization, substrate recognition, and oligomerization[29,30].

The molecular basis for the Ca^{2+} dependence of HpiC1 was demonstrated through two well-ordered binding sites near the enzyme active site. A paradoxical aspect of this calcium requirement is the observation that low millimolar concentrations of $CaCl_2$ caused HpiC1 to precipitate. This effect was reversible by stoichiometric addition of EDTA, indicative of calcium-dependent higher order oligomerization of HpiC1. However, a requirement for millimolar concentrations of Ca^{2+} in the reaction to achieve activity has been reported for some cyclases[18]. There are also fascinating instances of heteromeric association of some Stig cyclases leading to variant stereochemical outcomes of the products, compared to the products of their homomeric counterparts[17,18]. Taken together these data are indicative of an important, yet complex structural role for Ca^{2+} in Stig cyclase catalysis that may involve higher order oligomerization. Because HpiC1 could not be crystallized without supplemental $CaCl_2$, we examined the lattice contacts for evidence of additional calcium binding sites. In crystal forms 1 and 2, which required 200 mM Ca^{2+} in the well solution, we found two sites in which calcium could facilitate formation of higher-order complexes. We observed one fully occupied interfacial calcium ion far from the active site in crystal form 1 (Supplementary Fig. 29), and a second Ca^{2+} at half occupancy in unrelated crystal forms 1 and 2 (Supplementary Fig. 30). This Ca^{2+} is adjacent to the active sites indicating that a bridging calcium ion could influence the activity of cyclase oligomers. A functional role of higher order oligomerization in HpiC1 remains unclear as the addition of supplemental (1 – 20 mM) Ca^{2+} enhances the enzymatic activity of HpiC1, but is not required for turnover (Fig. 4). Further structural investigation will be required to understand the assembly of heteromeric Stig cyclase complexes, and the relevance of Ca^{2+} in those cases.

We have established the location of the HpiC1 active site, and using mutational analysis identified critical residues for catalysis and demonstrated a key relationship between amino acid sequence and product outcome. Most importantly, we identified D214 as the source of an active site acid that is required for catalysis, and is consistent with reports of acid catalyzed Cope rearrangements[24]. An active site acid is also consistent with the reported 3-fold increase in apparent k_{cat} as pH was decreased from 9.0

to 6.0 in the Stig cyclase WelU1 (68% sequence identity with HpiC1)[19]. Notably, the hydrophobic environment around D214 is essential to maintain a suitable population of the protonated species, as the Y101S/F138S mutation significantly reduced enzyme activity. We also identified a key regiochemical switch at F138 that gave rise to production of the fischerindole core in HpiC1. In these studies, the general importance of F138 in the HpiC1 homolog FimC5 was also confirmed, where a corresponding mutation also affected the product distribution with respect to regiochemistry (Supplementary Fig. 9). Together these findings will facilitate our efforts to anticipate the product profiles in new cyclases that are identified as additional strains and gene clusters are discovered.

We also explored the HpiC1 active site dynamics using a combination of DFT quantum mechanical calculations of mechanism and modes of catalysis, and MD simulations on the protein. We studied the origins of the three-part catalytic mechanism, and how HpiC1 controls the regiochemistry of product formation by favoring a particular conformation of substrate **1** and the reaction intermediate 4P. We have examined the role of key mutations in HpiC1 that switch the native product outcome from hapalindole **5** to fischerindole **6**. Together, these results address several of the catalytic steps in the formation of **5** from **1**(*R*). Further analysis will be required to establish the mechanistic basis by which the variant Stig cyclases achieve differentiation at the 6-*exo-trig* cyclization step, where the stereocenters at C10 and C15 are set (e.g. Hapalindole U, H, and J series) (Supplementary Fig. 1). Structural studies on additional Stig cyclases, mutational analysis across key active site residues, and computational modeling of the reaction intermediates will enable prediction of product profiles, and engineering of new selectivities to diversify further this remarkable family of natural products.

REFERENCES

1. Bhat, V., Dave, A., MacKay, J. A. & Rawal, V. H. The chemistry of hapalindoles, fischerindoles, ambiguines, and welwitindolinones. *Alkaloids Chem. Biol.* **73**, 65-160 (2014).
2. Asthana, R. K. *et al.* Identification of an antimicrobial entity from the cyanobacterium *Fischerella* sp. isolated from bark of *Azadirachta indica* (Neem) tree. *J. Appl. Phycol.* **18**, 33-39 (2006).
3. Becher, P. G., Keller, S., Jung, G., Sussmuth, R. D. & Juttner, F. Insecticidal activity of 12-*epi*-hapalindole J isonitrile. *Phytochemistry* **68**, 2493-2497 (2007).

4. Cagide, E. *et al.* Hapalindoles from the cyanobacterium *Fischerella*: Potential sodium channel modulators. *Chem. Res. Toxicol.* **27**, 1696-1706 (2014).
5. Mo, S., Krunic, A., Chlipala, G. & Orjala, J. Antimicrobial ambiguine isonitriles from the cyanobacterium *Fischerella ambigua*. *J. Nat. Prod.* **72**, 894-899 (2009).
6. Mo, S., Krunic, A., Santarsiero, B. D., Franzblau, S. G. & Orjala, J. Hapalindole-related alkaloids from the cultured cyanobacterium *Fischerella ambigua*. *Phytochemistry* **71**, 2116-2123 (2010).
7. Zhang, X. Q. & Smith, C. D. Microtubule effects of welwistatin, a cyanobacterial indolinone that circumvents multiple drug resistance. *Mol. Pharmacol.* **49**, 288-294 (1996).
8. Hillwig, M. L., Zhu, Q. & Liu, X. Biosynthesis of ambiguine indole alkaloids in cyanobacterium *Fischerella ambigua*. *ACS Chem. Biol.* **9**, 372-377 (2014).
9. Raveh, A. & Carmeli, S. Antimicrobial ambiguines from the cyanobacterium *Fischerella* sp. collected in Israel. *J. Nat. Prod.* **70**, 196-201 (2007).
10. Stratmann, K. *et al.* Welwitindolinones, unusual alkaloids from the blue-green algae *Hapalosiphon welwitschii* and *Westiella intricata*. Relationship to fischerindoles and hapalinodoles. *J. Am. Chem. Soc.* **116**, 9935-9942 (1994).
11. Li, S. *et al.* Hapalindole/ambiguine biogenesis is mediated by a Cope rearrangement, C–C bond-forming cascade. *J. Am. Chem. Soc.* **137**, 15366-15369 (2015).
12. Cope, A. C. & Hardy, E. M. The introduction of substituted vinyl groups. V. A rearrangement involving the migration of an allyl group in a three-carbon system. *J. Am. Chem. Soc.* **62**, 441-444 (1940).
13. Ilardi, E. A., Stivala, C. E. & Zakarian, A. [3,3]-sigmatropic rearrangements: Recent applications in the total synthesis of natural products. *Chem. Soc. Rev.* **38**, 3133-3148 (2009).
14. DeClue, M. S., Baldridge, K. K., Kunzler, D. E., Kast, P. & Hilvert, D. Isochorismate pyruvate lyase: A pericyclic reaction mechanism? *J. Am. Chem. Soc.* **127**, 15002-15003 (2005).
15. Luk, L. Y., Qian, Q. & Tanner, M. E. A Cope rearrangement in the reaction catalyzed by dimethylallyltryptophan synthase? *J. Am. Chem. Soc.* **133**, 12342-12345 (2011).
16. Tanner, M. E. Mechanistic studies on the indole prenyltransferases. *Nat. Prod. Rep.* **32**, 88-101 (2015).
17. Li, S. *et al.* Decoding cyclase-dependent assembly of hapalindole and fischerindole alkaloids. *Nat. Chem. Biol.* **13**, 467-469 (2017).
18. Zhu, Q. & Liu, X. Discovery of a calcium-dependent enzymatic cascade for the selective assembly of hapalindole-type alkaloids: On the biosynthetic origin of hapalindole U. *Angew. Chem. Int. Ed. Engl.* **56**, 9062-9066 (2017).
19. Zhu, Q. & Liu, X. Molecular and genetic basis for early stage structural diversifications in hapalindole-type alkaloid biogenesis. *Chem. Commun. (Camb.)* **53**, 2826-2829 (2017).
20. Krissinel, E. & Henrick, K. Inference of macromolecular assemblies from crystalline state. *J. Mol. Biol.* **372**, 774-797 (2007).
21. Holm, L. & Rosenstrom, P. Dali server: Conservation mapping in 3D. *Nucleic Acids Res.* **38**, W545-549 (2010).
22. von Schantz, L. *et al.* Structural basis for carbohydrate-binding specificity–a comparative assessment of two engineered carbohydrate-binding modules. *Glycobiology* **22**, 948-961 (2012).
23. Trott, O. & Olson, A. J. Autodock vina: Improving the speed and accuracy of docking with a new scoring function, efficient optimization, and multithreading. *J. Comput. Chem.* **31**, 455-461 (2010).
24. Lutz, R. P. Catalysis of the Cope and Claisen rearrangements. *Chem. Rev.* **84**, 205-247 (1984).
25. Wendt, K. U., Poralla, K. & Schulz, G. E. Structure and function of a squalene cyclase. *Science* **277**, 1811-1815 (1997).
26. Starks, C. M., Back, K., Chappell, J. & Noel, J. P. Structural basis for cyclic terpene biosynthesis by tobacco 5-epi-aristolochene synthase. *Science* **277**, 1815-1820 (1997).
27. Lesburg, C. A., Zhai, G., Cane, D. E. & Christianson, D. W. Crystal structure of pentalenene synthase: Mechanistic insights on terpenoid cyclization reactions in biology. *Science* **277**, 1820-1824 (1997).

28. Jenson, C. & Jorgensen, W. L. Computational investigations of carbenium ion reactions relevant to sterol biosynthesis. *J. Am. Chem. Soc.* **119**, 10846-10854 (1997).
29. Abou-Hachem, M. *et al.* Calcium binding and thermostability of carbohydrate binding module CBM4-2 of Xyn10A from *Rhodothermus marinus*. *Biochemistry* **41**, 5720-5729 (2002).
30. Montanier, C. Y. *et al.* A novel, noncatalytic carbohydrate-binding module displays specificity for galactose-containing polysaccharides through calcium-mediated oligomerization. *J. Biol. Chem.* **286**, 22499-22509 (2011).

ONLINE METHODS

Cloning and mutagenesis of HpiC1 and FimC5. HpiC1 and FimC5 were cloned into pET28 (Novagen) from codon optimized synthetic genes (IDT gBlocks®) with their N-terminal leader peptides truncated[17]. Site-directed mutagenesis of HpiC1 and FimC5 was performed using a single primer method based on "Quikchange" mutagenesis (Agilent Genomics). Mutagenic primer sequences are listed in Supplementary Table 2. All mutations were verified by DNA sequencing at the University of Michigan DNA Sequencing Core.

Expression of HpiC1 and FimC5 proteins. HpiC1 and FimC5 and their corresponding active site mutants were overexpressed in *Escherichia coli* strain BL21 (DE3). Cultures from a single colony were used to inoculate 1.5 L terrific broth (TB) supplemented with 50 μg/mL kanamycin. Expression was induced with 0.7 mM isopropyl-β-D-thiogalactopyranoside when cultures reached OD_{600} ~ 1.0. After 20 h induction at 18 °C the cells were harvested by centrifugation and stored at -80 °C.

Expression of HpiC1 W73M/K132M selenomethionine derivative. An initial challenge involved the lack of native methionine residues in HpiC1. Therefore, a series of mutants containing methionine substitutions were screened for crystallization. Sites for substitution were selected based on positions containing a native methionine in sequence comparisons with other Stig cyclases. Selenomethionine (SeMet) HpiC1 W73M/K132M was produced by metabolic inhibition[31]. Briefly, freshly transformed BL21 (DE3) cells harboring the hpiC1 gene on pET28 were used to incolulate 3 L M9 minimal medium supplemented with 50 μg/mL kanamycin. An amino acid cocktail containing L-selenomethionine was added when the cells reached OD_{600} = 1.0. The cells were cooled to 18 °C and shaken for 30 min prior to

induction with 0.7 mM isopropyl-β-D-thiogalactopyranoside. After 20 h induction the cells were harvested by centrifugation and stored at -80 °C.

Purification of recombinant proteins. All proteins were purified as described previously[17]. Briefly, 10 g *E. coli* wet cell mass containing the recombinant cyclase was resuspended in 75 mL lysis buffer (10 mM HEPES pH 7.6, 50 mM NaCl, 10% glycerol). Cells were lysed by the addition of lysozyme (0.5 mg/mL) and sonication and clarified by centrifugation at 60,000 x*g* for 25 min. Clarified lysate was loaded by gravity onto 8 mL NiNTA Superflow resin (Qiagen). The column was washed with 100 mL lysis buffer containing 20 mM imidazole and 50 mL lysis buffer containing 40 mM imidazole. The proteins were eluted with elution buffer (250 mM imidazole, pH 7.9 and 10% glycerol). Fractions containing the purified cyclase were concentrated using Amicon Ultra 15 centrifugal filters and desalted using PD-10 columns (GE Healthcare) equilibrated with storage buffer (10 mM HEPES pH 7.6, 50 mM NaCl). The purified cyclases were drop-frozen in 30 µL aliquots directly into liquid N_2 and stored at -80 °C.

Crystallization of SeMet HpiC1 W73M/K132M. Single, diffraction quality crystals of the HpiC1 W73M/K132M selenomethionine derivative were grown in Intelli-Plate 96-2 shallow well plates (Hampton research) at 20 °C by mixing 1 µL of 11 mg/mL SeMet HpiC1 in storage buffer with 1 µL of a well solution containing 23% PEG 3350, 200 mM $CaCl_2$, 5% trehalose. Sitting droplets were nucleated after 18 h from an earlier spontaneous crystallization event using a cat whisker. Single, rod-shaped crystals grew to approximate dimensions of 50 x 50 x 250 µm after 14 days. 8 µL of a cryoprotecting solution containing 10 mM HEPES pH 7.6, 50 mM NaCl, 23% PEG 3350, 200 mM $CaCl_2$, 9.1% trehalose was added directly to the sitting drops and the crystals were harvested using nylon loops and vitrified by rapid plunging into liquid nitrogen. SeMet HpiC1 crystallized in Form 1, space group $P2_12_12_1$ with unit cell dimensions of a = 44.9 Å, b = 81.1 Å, c = 131.7 Å, and two chains in the asymmetric unit.

Crystallization of Native HpiC1 ($P4_2$). Single, diffraction quality crystals of HpiC1 native were grown in Intelli-Plate 96-2 shallow well plates (Hampton research) at 20 °C by mixing 1 µL of 20 mg/mL HpiC1 in storage buffer with 1 µL of a well solution containing 22% PEG 4000, 200 mM $CaCl_2$, 100 mM Tris pH 8.5, 5% ethylene glycol. Sitting droplets were nucleated after 4 h from an earlier spontaneous

crystallization event using a cat whisker. Single, rod-shaped crystals grew to approximate dimensions of 50 x 50 x 150 μm after 7 days. 8 μL of a cryoprotecting solution containing 10 mM HEPES pH 7.6, 50 mM NaCl, 22% PEG 4000, 200 mM $CaCl_2$, 100 mM Tris pH 8.5, 15% ethylene glycol was added directly to the sitting drops and the crystals were harvested using nylon loops and vitrified by rapid plunging into liquid nitrogen. In these conditions, HpiC1 native crystallized in Form 2, space group $P4_2$ with unit cell dimensions of a = 71.3 Å, b = 71.3 Å, c = 80.6 Å, and two chains in the asymmetric unit.

Crystallization of Native HpiC1 (C2). Single, diffraction quality crystals of HpiC1 native were grown in Intelli-Plate 96-2 shallow well plates (Hampton research) at 20 °C by mixing 1 μL of 20 mg/mL HpiC1 in storage buffer and 5% DMSO with 1 μL of a well solution containing 22% PEG 4000, 150 mM $CaCl_2$, 100 mM Tris pH 8.5, 5% ethylene glycol. Sitting droplets were nucleated after 4 h from an earlier spontaneous crystallization event using a cat whisker. Single, diamond-shaped crystals grew to approximate dimensions of 200 x 200 x 100 μm after 7 days. 8 μL of a cryoprotecting solution containing 10 mM HEPES pH 7.6, 50 mM NaCl, 22% PEG 4000, 150 mM $CaCl_2$, 100 mM Tris pH 8.5, 15% ethylene glycol, 5% DMSO was added directly to the sitting drops and the crystals were harvested using nylon loops and vitrified by rapid plunging into liquid nitrogen. In these conditions, HpiC1 native crystallized in Form 3, space group $C2$ with unit cell dimensions of a = 113.8 Å, b = 49.5 Å, c = 53.1 Å, α = 90°, β = 110.5°, γ = 90° and one chain in the asymmetric unit.

Crystallization of HpiC1 Y101F. Single, diffraction quality crystals of HpiC1 Y101F were grown in Intelli-Plate 96-2 shallow well plates (Hampton research) at 20 °C by mixing 1 μL of 15 mg/mL protein in storage buffer with 1 μL of a well solution containing 22% PEG 4000, 150 mM $CaCl_2$, 100 mM Tris pH 8.5, 5% ethylene glycol. Sitting droplets were nucleated after 4 h from an earlier spontaneous crystallization event using a cat whisker. Single, diamond-shaped crystals grew to approximate dimensions of 250 x 250 x 270 μm after 7 days. 8 μL of a cryoprotecting solution containing 10 mM HEPES pH 7.6, 50 mM NaCl, 22% PEG 4000, 150 mM $CaCl_2$, 100 mM Tris pH 8.5, 15% ethylene glycol was added directly to the sitting drops and the crystals were harvested using nylon loops and vitrified by rapid plunging into liquid nitrogen. HpiC1 Y101F crystallized in Form 3, space group $C2$ with unit cell

dimensions of a = 113.8 Å, b = 49.8 Å, c = 53.4 Å, α = 90°, β = 110.4°, γ = 90° and one chain in the asymmetric unit.

Crystallization of HpiC1 Y101S. Single, diffraction quality crystals of HpiC1 Y101S were grown in Intelli-Plate 96-2 shallow well plates (Hampton research) at 20 °C by mixing 1 µL of 15 mg/mL protein in storage buffer with 1 µL of a well solution containing 20% MEPEG 5000, 150 mM $CaCl_2$, 100 mM Tris pH 8.5, 5% ethylene glycol. Sitting droplets were nucleated after 4 h from an earlier spontaneous crystallization event using a cat whisker. Single, diamond-shaped crystals grew to approximate dimensions of 250 x 250 x 270 µm after 7 days. 8 µL of a cryoprotecting solution containing 10 mM HEPES pH 7.6, 50 mM NaCl, 20% MEPEG 5000, 150 mM $CaCl_2$, 100 mM Tris pH 8.5, 15% ethylene glycol, 5% DMSO was added directly to the sitting drops and the crystals were harvested using nylon loops and vitrified by rapid plunging into liquid nitrogen. HpiC1 Y101S crystallized in Form 3, space group $C2$ with unit cell dimensions of a = 113.9 Å, b = 49.6 Å, c = 53.4 Å, α = 90°, β = 110.3°, γ = 90° and one chain in the asymmetric unit.

Crystallization of HpiC1 F138S and Y101F/F138S. Single, diffraction quality crystals of HpiC1 F138S and Y101F/F138S were grown in Intelli-Plate 96-2 shallow well plates (Hampton research) at 20 °C by mixing 1 µL of 15 mg/mL protein in storage buffer, 20 mM $CaCl_2$, 5% DMSO with 1 µL of a well solution containing 20% MEPEG 5000, 100 mM BisTris pH 6.5, 5% ethylene glycol. Sitting droplets were nucleated after 4 h from an earlier spontaneous crystallization event using a cat whisker. Single, plate-shaped crystals grew to approximate dimensions of 50 x 50 x 300 µm after 7 days. 8 µL of a cryoprotecting solution containing 10 mM HEPES pH 7.6, 50 mM NaCl, 20% MEPEG 5000, 20 mM $CaCl_2$, 100 mM BisTris pH 6.5, 15% ethylene glycol, 5% DMSO was added directly to the sitting drops and the crystals were harvested using nylon loops and vitrified by rapid plunging into liquid nitrogen. HpiC1 F138S and HpiC1 Y101F/F138S crystallized in Form 4, space group $P2_1$ with unit cell dimensions of a = 62.0 Å, b = 47.9 Å, c = 174.2 Å, α = 90°, β = 97.2°, γ = 90° and four chains in the asymmetric unit.

Data collection and processing. X-ray data were collected at 100 K on beamline 23ID-B at the General Medical Sciences and Cancer Institutes Structural Biology Facility at the Advanced Photon Source in

Argonne, IL, USA. Diffraction data were integrated and scaled using XDS[32]. Data collection statistics are given in Supplementary Table 1.

Experimental phasing (SAD) and molecular replacement, model building and refinement. The structure of SeMet HpiC1 W73M/K132M was solved using single wavelength anomalous diffraction (SAD). Phasing and initial model building were performed using Phenix Autosol[33]. This resulted in an initial model that could be extended by alternating cycles of manual building in *Coot*[34] and least-squares refinement with Refmac[35]. The structures for HpiC1 native and Y101F, Y101S, F138S, Y101F/F138S were solved by molecular replacement using Phaser-MR[36] with the structure of the HpiC1 selenomethionine derivative as a search model. Final models were generated by alternating cycles of manual building in *Coot*[34] and refinement in Refmac[35] and Phenix[33], and were validated using MolProbity[37].

Docking 12-epi-hapalindole U with Autodock VINA. 12-*epi*-hapalindole U was docked into the SeMet HpiC1 model using Autodock VINA[23]. Default parameters for Autodock VINA were used with the exception of exhaustiveness, which was set to 100.

Molecular graphics. All figures depicting the protein structure were generated with PyMOL (Version 1.8 Schrödinger, LLC).

Chemical synthesis. Indole isonitrile was synthesized as described previously[11].

In vitro cyclase assays. In vitro assays were performed with HpiC1, FimC5 and their corresponding active site mutants as described previously[17]. Briefly, FamD2, GPP, Indole isonitrile, cyclase, $CaCl_2$. Products were analyzed using LC/MS (Shimadzu) using C18 (Agilent) HPLC column and monitored by UV absorbance at 280 nm.

Scaleup, purification, and NMR of F138S product (12-epi-fischerindole U). The semi-prep scale reaction was performed as described previously[17].

Quantum mechanical calculations. Conformational searches of the hapalindole and fischerindole products were performed using the Schrödinger MacroModel software package (Release 2017-2, Schrödinger, LLC), and the lowest energy conformation was used for all reported quantum mechanical calculations. All quantum mechanical calculations were performed using the Gaussian 09 (Revision A.02, Gaussian,

Inc.) software package. Structures were optimized in the gas phase at the B3LYP[38,39]/6-31G(d) level of theory; frequency calculations were used to confirm the presence of local minima (no imaginary frequencies) and transition states (one imaginary frequency) and to calculate free energies at 298 K. To obtain more accurate energetics, single-point energy calculations were performed on the optimized structures at the B3LYP/6-311++G(d,p) level of theory using Grimme's D3(BJ) dispersion correction[40,41] and the IEFPCM[42-44] solvent model for diethyl ether ($\varepsilon = 4$). The use of the dielectric constant ε=4 has proven to be a good model to estimate the dielectric permittivity in the enzyme active site, accounting for electronic polarization and small backbone fluctuations[45,46].

Molecular dynamics simulations. Molecular dynamics simulations were performed using the GPU code (*pmemd*)[47] of the AMBER 16 package (AMBER 2016, University of California). Parameters for intermediates and substrates were generated within the *antechamber* module using the general AMBER force field (*gaff*)[48], with partial charges set to fit the electrostatic potential generated at the HF/6-31G(d) level by the RESP model[49]. The charges were calculated according to the Merz–Singh–Kollman scheme[50,51] using the Gaussian 09 package (Revision A.02, Gaussian, Inc.). Each protein was immersed in a pre-equilibrated truncated cuboid box with a 10 Å buffer of TIP3P[52] water molecules using the *leap* module, resulting in the addition of around 15,000 solvent molecules. The systems were neutralized by addition of explicit counter ions (Na^+ and Cl^-). All subsequent calculations were done using the widely tested Stony Brook modification of the Amber14 force field (*ff14sb*)[53]. A two-stage geometry optimization approach was performed. The first stage minimizes the positions of solvent molecules and ions imposing positional restraints on the solute by a harmonic potential with a force constant of 500 $kcal \cdot mol^{-1} \cdot Å^{-2}$ and the second stage minimizes all the atoms in the simulation cell. The systems were gently heated using six 50 ps steps, incrementing the temperature by 50 K for each step (0–300 K) under constant-volume and periodic-boundary conditions. Water molecules were treated with the SHAKE algorithm such that the angle between the hydrogen atoms was kept fixed. Long-range electrostatic effects were modelled using the particle-mesh-Ewald method[54]. An 8 Å cutoff was applied to Lennard–Jones and electrostatic interactions. Harmonic restraints of 10 $kcal \cdot mol^{-1}$ were applied to the solute and

the Langevin equilibration scheme was used to control and equalize the temperature. The time step was kept at 1 fs during the heating stages, allowing potential inhomogeneities to self-adjust. Each system was then equilibrated without restrains for 2 ns with a 2 fs time step at a constant pressure of 1 atm and temperature of 300 K. After the systems were equilibrated in the NPT ensemble, subsequent MD simulations were performed for an additional 500 ns under an NVT ensemble and periodic-boundary conditions.

METHODS REFERENCES

31. Van Duyne, G. D., Standaert, R. F., Karplus, P. A., Schreiber, S. L. & Clardy, J. Atomic structures of the human immunophilin FKBP-12 complexes with FK506 and rapamycin. *J. Mol. Biol.* **229**, 105-124 (1993).
32. Kabsch, W. XDS. *Acta Crystallogr. D. Biol. Crystallogr.* **66**, 125-132 (2010).
33. Adams, P. D. *et al.* PHENIX: A comprehensive python-based system for macromolecular structure solution. *Acta Crystallogr. D. Biol. Crystallogr.* **66**, 213-221 (2010).
34. Emsley, P., Lohkamp, B., Scott, W. G. & Cowtan, K. Features and development of Coot. *Acta Crystallogr. D. Biol. Crystallogr.* **66**, 486-501 (2010).
35. Murshudov, G. N. *et al.* REFMAC5 for the refinement of macromolecular crystal structures. *Acta Crystallogr. D. Biol. Crystallogr.* **67**, 355-367 (2011).
36. McCoy, A. J. *et al.* Phaser crystallographic software. *J. Appl. Crystallogr.* **40**, 658-674 (2007).
37. Chen, V. B. *et al.* MolProbity: all-atom structure validation for macromolecular crystallography. *Acta Crystallogr. D. Biol. Crystallogr.* **66**, 12-21 (2010).
38. Becke, A. D. Density-functional thermochemistry. III. The role of exact exchange. *J. Chem. Phys.* **98**, 5648-5652 (1993).
39. Lee, C. T., Yang, W. T. & Parr, R. G. Development of the Colle-Salvetti correlation-energy formula into a functional of the electron-density. *Phys. Rev. B: Condens. Matter* **37**, 785-789 (1988).
40. Grimme, S., Antony, J., Ehrlich, S. & Krieg, H. A consistent and accurate ab initio parametrization of density functional dispersion correction (DFT-D) for the 94 elements H-Pu. *J. Chem. Phys.* **132**, 154104 (2010).
41. Grimme, S., Ehrlich, S. & Goerigk, L. Effect of the damping function in dispersion corrected density functional theory. *J. Comput. Chem.* **32**, 1456-1465 (2011).
42. Miertuš, S., Scrocco, E. & Tomasi, J. Electrostatic interaction of a solute with a continuum. A direct utilizaion of ab initio molecular potentials for the prevision of solvent effects. *Chem. Phys.* **55**, 117-129 (1981).
43. Miertus, S. & Tomasi, J. Approximate evaluations of the electrostatic free-energy and internal energy changes in solution processes. *Chem. Phys.* **65**, 239-245 (1982).
44. Pascual-ahuir, J. L., Silla, E. & Tuñon, I. GEPOL: An improved description of molecular surfaces. III. A new algorithm for the computation of a solvent-excluding surface. *J. Comput. Chem.* **15**, 1127-1138 (1994).
45. Li, L., Li, C., Zhang, Z. & Alexov, E. On the dielectric "constant" of proteins: smooth dielectric function for macromolecular modeling and its implementation in DelPhi. *J. Chem. Theory Comput.* **9**, 2126-2136 (2013).
46. Schutz, C. N. & Warshel, A. What are the dielectric "constants" of proteins and how to validate electrostatic models? *Proteins* **44**, 400-417 (2001).

47. Salomon-Ferrer, R., Gotz, A. W., Poole, D., Le Grand, S. & Walker, R. C. Routine microsecond molecular dynamics simulations with AMBER on GPUs. 2. Explicit solvent particle mesh Ewald. *J. Chem. Theory Comput.* **9**, 3878-3888 (2013).
48. Wang, J., Wolf, R. M., Caldwell, J. W., Kollman, P. A. & Case, D. A. Development and testing of a general amber force field. *J. Comput. Chem.* **25**, 1157-1174 (2004).
49. Bayly, C. I., Cieplak, P., Cornell, W. D. & Kollman, P. A. A well-behaved electrostatic potential based method using charge restraints for deriving atomic charges - the RESP model. *J. Phys. Chem.* **97**, 10269-10280 (1993).
50. Besler, B. H., Merz, K. M. & Kollman, P. A. Atomic charges derived from semiempirical methods. *J. Comput. Chem.* **11**, 431-439 (1990).
51. Singh, U. C. & Kollman, P. A. An approach to computing electrostatic charges for molecules. *J. Comput. Chem.* **5**, 129-145 (1984).
52. Jorgensen, W. L., Chandrasekhar, J., Madura, J. D., Impey, R. W. & Klein, M. L. Comparison of simple potential functions for simulating liquid water. *J. Chem. Phys.* **79**, 926-935 (1983).
53. Maier, J. A. *et al.* Ff14sb: Improving the accuracy of protein side chain and backbone parameters from ff99sb. *J. Chem. Theory Comput.* **11**, 3696-3713 (2015).
54. Darden, T., York, D. & Pedersen, L. Particle mesh Ewald: An $N\cdot\log(N)$ method for Ewald sums in large systems. *J. Chem. Phys.* **98**, 10089-10092 (1993).

ACCESSION CODES

The atomic coordinates and structure factors have been deposited with the Research Collaboratory for Structural Bioinformatics as Protein Data Bank entries 5WPP, 5WPR, 6AL6, 5WPR, 5WPU, 6AL7, and 6AL8 (www.rcsb.org).

ACKNOWLEDGMENTS

The authors thank the National Science Foundation under the CCI Center for Selective C-H Functionalization (CHE-1700982), the National Institutes of Health (CA70375 to R.M.W. and D.H.S.), R35 GM118101, and the Hans W. Vahlteich Professorship (to D.H.S.) for financial support. M.G.-B. thanks the Ramón Areces Foundation for a postdoctoral fellowship. J.N.S. acknowledges the support of the National Institute of General Medical Sciences of the National Institutes of Health under Award Number F32GM122218. Computational resources were provided by the UCLA Institute for Digital Research and Education (IDRE) and the Extreme Science and Engineering Discovery Environment (XSEDE), which is supported by the NSF (OCI-1053575). The content does not necessarily represent the official views of the National Institutes of Health.

AUTHOR CONTRIBUTIONS

S.A.N. conducted protein preparation and crystallography. S.L. cloned the genes and assayed the enzymes. M.G.-B. conducted MD simulations. J.N.S. conducted DFT calculations. A.N.L synthesized substrates. F.Y. performed bioinformatics analyses. S.A.N., S.L., M.G.-B., J.N.S, S.Y., J.L.S, R.M.W., K.N.H and D.H.S designed research and conducted data analysis and interpretation. S.A.N., S.L., M.G.-B., J.N.S, J.L.S, K.N.H and D.H.S wrote the manuscript.

COMPETING FINANCIAL INTERESTS

The authors declare no competing financial interests.

FIGURE LEGENDS

Fig. 1. Biogenesis of hapalindole alkaloids. The hapalindole and fischerindole core ring systems arise from the common biosynthetic intermediate **1**. Stig cyclases catalyze a Cope rearrangement followed by cyclization to generate tetracyclic products and trace levels of tri-cyclic shunt products. HpiC1 catalyzes formation of **5**, while FimC5 catalyzes formation of **6**, with identical stereochemistry at C11 and C12, but different C-ring regiochemistry.

Fig. 2. HpiC1 structure overview at 1.5 Å. (**a**) Cartoon representation of HpiC1 homodimer; the subunits are colored blue and magenta, green spheres indicate bound calcium ions. (**b**) Surface representation colored by atom of a single protomer shows 2060 $Å^2$ buried surface area between the subunits. (**c**) Superposition of xylanase CBM homolog (PDB id: 2Y64, rainbow); CBM is monomeric despite sharing the same fold as HpiC1.

Fig. 3. Active site of SeMet HpiC1 W73M/K132M. (**a**) Surface representation of the SeMet HpiC1 active site. Key residues are shown as green sticks. Met73 is substituted for the native tryptophan residue. This mutant protein retained wild-type activity (**b**) Key active site residues shown in an alignment with other Stig cyclases. Residues are colored by conservation and side chain composition (ClustalX).

Fig. 4. In vitro characterization of HpiC1 mutants using **1** as substrate. Substitution of the catalytic acid D214 to alanine abolished activity. A single mutation F138S altered the native product profile of HpiC1 to produce **6**. The product became predominantly **6** in the HpiC1 Y101F/F138S double mutant. Products were monitored by UV and confirmed using ^{1}H-NMR.

Fig. 5. QM analysis. (**a**) Cope rearrangement, 6-*exo*-*trig* cyclization, and electrophilic aromatic substitution cascade starting from the (*R*)-enantiomer of substrate **1** in a near attack conformation and leading to **5** precursor 5P and **6** precursor 6P. The energetics of the Cope rearrangement are computed with the neutral indolenine (pathway N), the *N*-protonated indolenine (pathway P), and the indolenine forming a hydrogen bond with acetic acid (pathway A). (**b**) Optimized geometry of key intermediate 4P that undergoes regioselective electrophilic aromatic substitution to form **5** or **6**.

Fig. 6. MD simulations of the active site. Representative snapshots of: (**a**) substrate 1(*R*)P (*violet*) bound into HpiC1; (**b**) Dihedral angles explored during the 500 ns of MD simulation for substrate 1(*R*)P bound into HpiC1. Dihedral-1 (N(NC) – C11 – C3 – C2) and dihedral-2 (C(Me-C12) – C12 – C3 – C2) define the relative orientation of substituents at C11 and C12 positions, respectively, during the MD simulation. The right axis indicates the final stereochemistry of C11 and C12 expected after the Cope rearrangement coming from the given near attack conformation (NAC) of 1(*R*)P, as shown in (**b**) and Supplementary Fig. 22. 1(*R*)P mainly explores one conformation during the MD trajectory leading to (*R*) configuration at C11 and (*S*) configuration at C12.

Representative snapshots obtained from 500 ns MD simulations of the active site for intermediate 4P bound to (**c**) HpiC1 (Supplementary Fig. 23-24); and (**d**) F138S (Supplementary Fig. 26). Distances (in Å) show that the conformation adopted by intermediate 4P in the HpiC1 wild-type enzyme moves C16 closer to C4 to form the hapalindole product, while the F138S mutant enables the exploration of a conformation of intermediate 4P in which C16 gets closer to C2 to allow fischerindole product formation.

Graphical Abstract

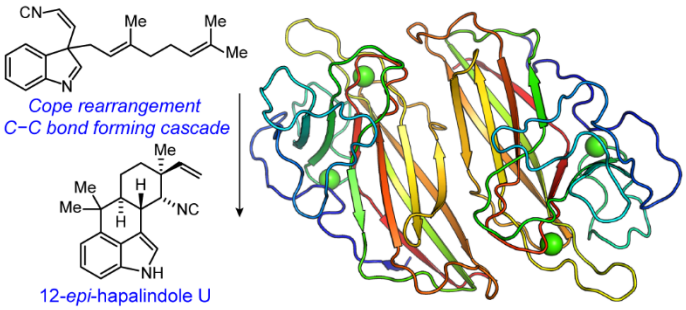

Fig.1

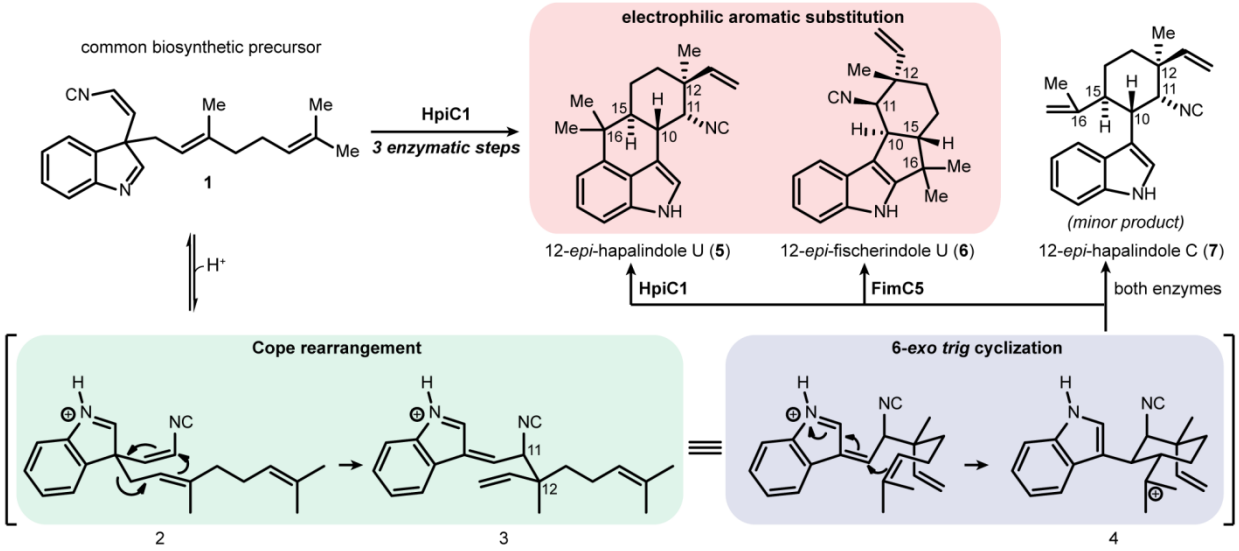
common biosynthetic precursor
1
HpiC1
3 enzymatic steps
electrophilic aromatic substitution
12-epi-hapalindole U (5)
12-epi-fischerindole U (6)
12-epi-hapalindole C (7)
(minor product)
HpiC1
FimC5
both enzymes
Cope rearrangement
6-exo trig cyclization
2
3
4

Fig. 2

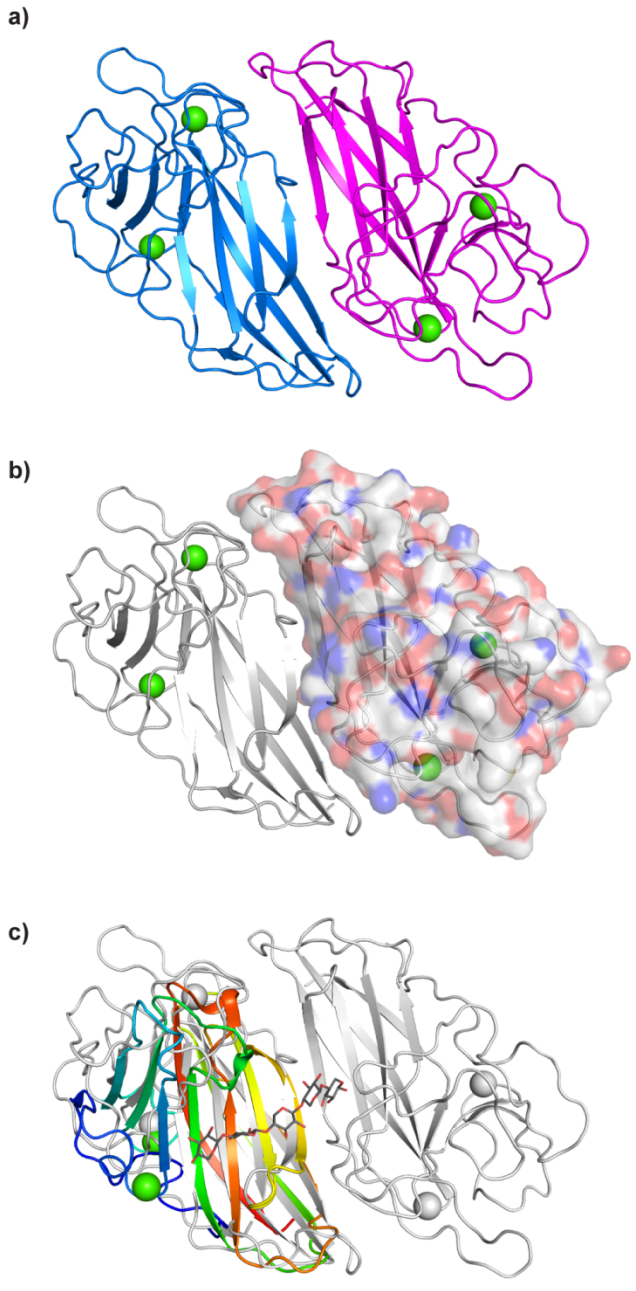

Fig. 3

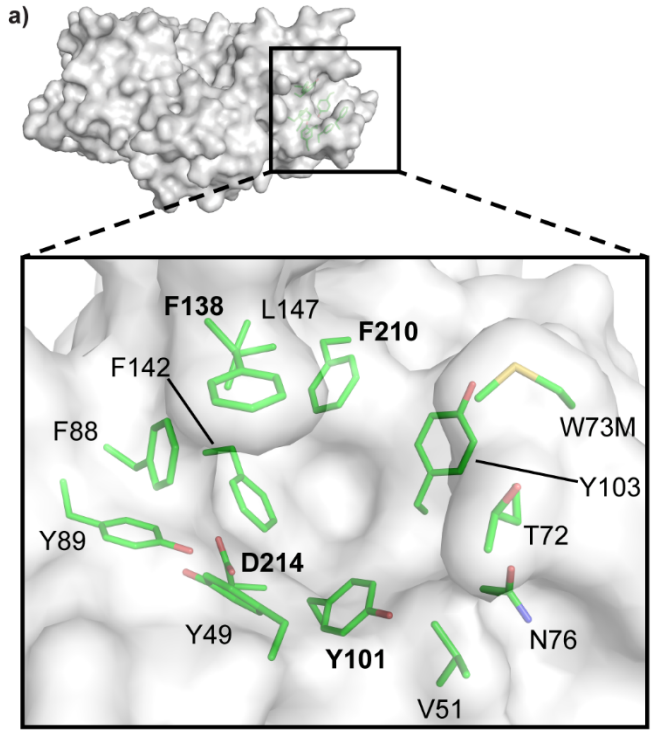

b)

	Y49	V51	T72	W73	N76	F88	Y89	Y101	Y103	F138	F142	L147	F210	D214
HpiC1	Y	V	TW	N	FY	Y	Y	F	F	L	F	D
FamC1	Y	I	TW	N	FY	Y	Y	L	F	F	F	D
FilC1	Y	V	TW	N	FY	Y	Y	L	F	F	F	D
FimC1	Y	I	TW	N	FY	Y	Y	L	F	F	F	D
HpiC2	Y	I	KW	N	FY	F	Y	F	F	F	F	D
FamC2	Y	I	KW	N	FY	F	Y	F	F	F	F	D
FilC2	Y	I	KW	N	FY	F	Y	F	F	F	F	D
FimC2	Y	I	KW	N	FY	F	Y	F	F	F	F	D
HpiC3	Y	V	VQ	Y	FY	S	Y	S	Y	L	S	D
FamC3	Y	V	VQ	Y	FY	S	Y	S	Y	L	S	D
FilC3	Y	V	VQ	Y	YY	S	Y	S	Y	L	S	D
FimC3	Y	V	VQ	Y	FY	S	Y	-	-	-	-	-
HpiC4	F	L	DS	Y	FY	S	Y	A	F	L	S	D
FamC4	F	L	NS	Y	FY	S	Y	A	F	L	S	D
FilC4	F	L	DS	Y	FY	S	Y	A	F	L	S	D
FimC4	F	L	DS	Y	FY	S	Y	A	F	L	S	D
HpiC5	Y	I	RI	N	FY	F	Y	S	F	L	F	D
FimC5	Y	I	RI	N	FY	F	Y	S	F	L	F	D

Fig. 4

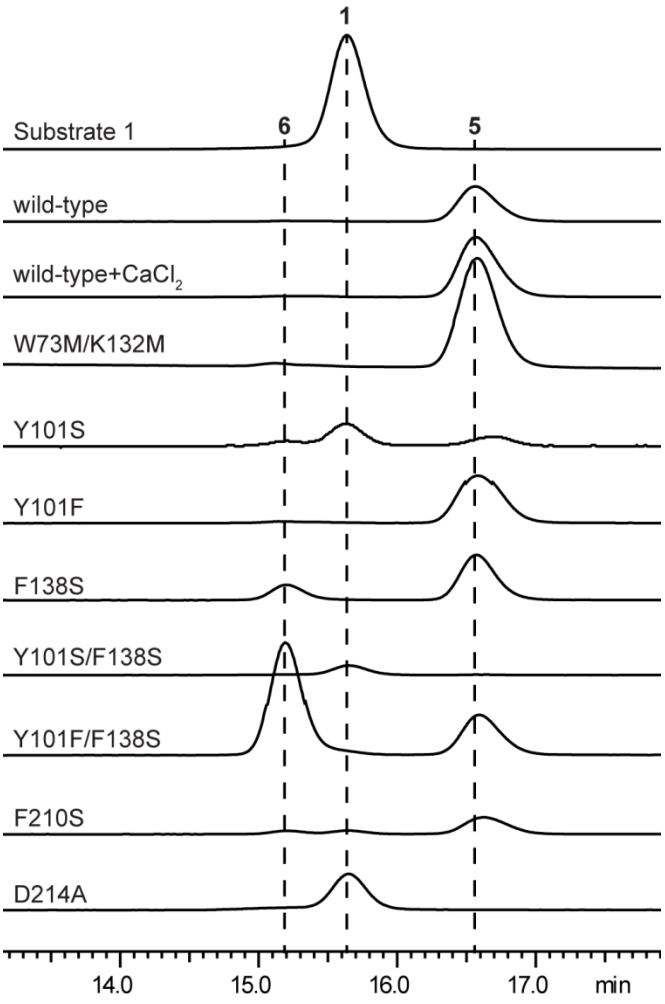
1
6
5
Substrate 1
wild-type
wild-type+CaCl2
W73M/K132M
Y101S
Y101F
F138S
Y101S/F138S
Y101F/F138S
F210S
D214A
14.0
15.0
16.0
17.0
min

Fig. 5

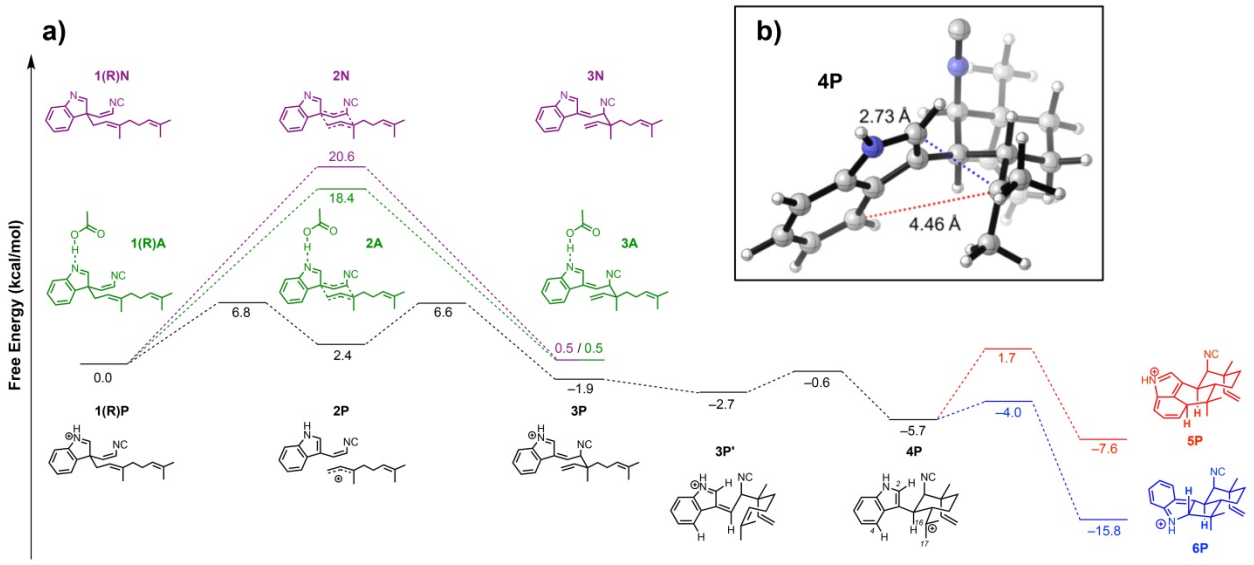
a)
b)
Free Energy (kcal/mol)
1(R)N
2N
3N
1(R)A
2A
3A
1(R)P
2P
3P
3P'
4P
5P
6P
20.6
18.4
6.8
6.6
2.4
0.0
0.5 / 0.5
−1.9
−2.7
−0.6
−5.7
1.7
−4.0
−7.6
−15.8
4P
2.73 Å
4.46 Å

Fig. 6

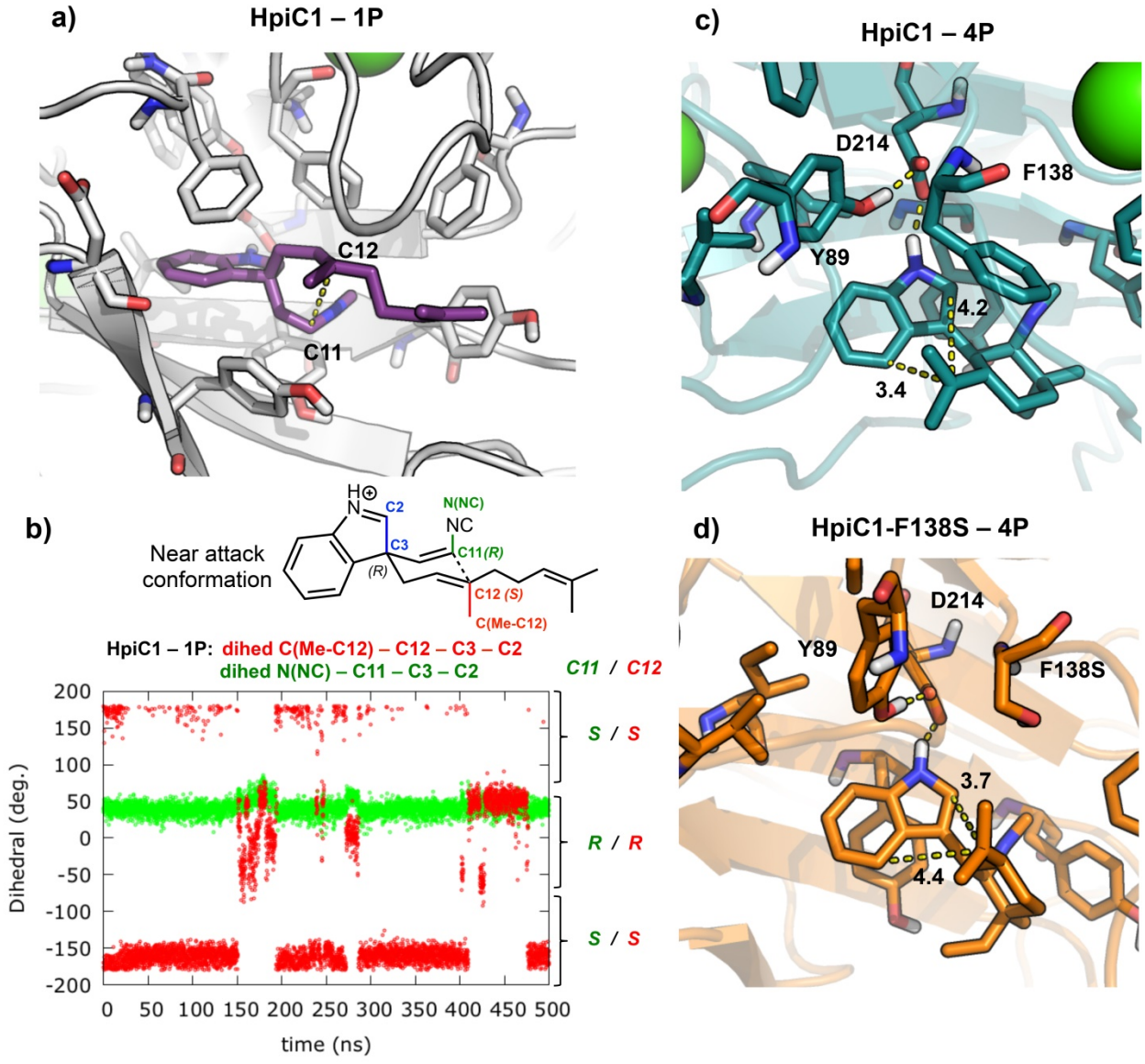
a)
HpiC1 – 1P
C12
C11
b)
Near attack conformation
HiP
N
C2
C3
N(NC)
NC
C11(R)
(R)
C12 (S)
C(Me-C12)
HpiC1 – 1P: dihed C(Me-C12) – C12 – C3 – C2
dihed N(NC) – C11 – C3 – C2
C11 / C12
S / S
R / R
S / S
Dihedral (deg.)
200
150
100
50
0
-50
-100
-150
-200
0 50 100 150 200 250 300 350 400 450 500
time (ns)
c)
HpiC1 – 4P
D214
F138
Y89
4.2
3.4
d)
HpiC1-F138S – 4P
D214
Y89
F138S
3.7
4.4